

LITHIUM INVENTORY OF $2M_{\odot}$ RED CLUMP STARS IN OPEN CLUSTERS: A TEST OF THE HELIUM FLASH MECHANISM

JOLEEN K. CARLBERG^{1, 4}, KATIA CUNHA², VERNE V. SMITH³

¹NASA Goddard Space Flight Center, Code 667, Greenbelt, MD 20771, USA joleen.k.carlberg@nasa.gov.

²Observatório Nacional, Rua General José Cristino, 77, 20921-400 São Cristóvão, Rio de Janeiro, RJ, Brazil

³National Optical Astronomy Observatory, 950 North Cherry Avenue, Tucson, AZ 85719, USA

⁴NASA Postdoctoral Program Fellow, joleen.k.carlberg@nasa.gov

ABSTRACT

The temperature distribution of field Li-rich red giants suggests the presence of a population of Li-rich red clump (RC) stars. One proposed explanation for this population is that all stars with masses near $2 M_{\odot}$ experience a short-lived phase of Li-richness at the onset of core He-burning. Many of these stars have low $^{12}\text{C}/^{13}\text{C}$, a signature of deep mixing that is presumably associated with the Li regeneration. To test this purported mechanism of Li enrichment, we measured abundances in 38 RC stars and 6 red giant branch (RGB) stars in four open clusters selected to have RC masses near $2 M_{\odot}$. We find six Li-rich stars ($A(\text{Li}) \geq 1.50$ dex) of which only two may be RC stars. None of the RC stars have Li exceeding the levels observed in the RGB stars, but given the brevity of the suggested Li-rich phase and the modest sample size, it is probable that stars with larger Li-enrichments were missed simply by chance. However, we find very few stars in our sample with low $^{12}\text{C}/^{13}\text{C}$. Such low $^{12}\text{C}/^{13}\text{C}$, seen in many field Li-rich stars, should persist even after lithium has returned to normal low levels. Thus, if Li synthesis during the He flash occurs, it is a rare, but potentially long-lived occurrence rather than a short-lived phase for all stars. We estimate a conservative upper limit of the fraction of stars going through a Li-rich phase to be $< 47\%$, based on stars that have low $^{12}\text{C}/^{13}\text{C}$ for their observed $A(\text{Li})$.

Keywords: open clusters and associations: individual (Collinder 110, NGC 2204, NGC 2506, NGC 6583) - stars: abundances - stars: late-type

1. INTRODUCTION

A small fraction of red giant stars have lithium abundances ($A(\text{Li})$) exceeding the predictions of standard evolution models even though the majority of red giants (RGs) exhibit $A(\text{Li})$ orders of magnitude below standard model predictions (Brown et al. 1989). The low $A(\text{Li})$ demonstrates that non-convective mixing processes contribute significantly to Li depletion, which makes the Li-rich stars appear even more unusual. The most Li-rich RGs have abundances exceeding the meteoritic abundances (Balachandran et al. 2000, Kumar & Reddy 2009, Adamów et al. 2015) and require a nucleosynthetic origin for the Li. Cameron & Fowler (1971) described a pathway for Li nucleosynthesis through the reactions $^3\text{He}(\alpha, \gamma)^7\text{Be}$ and $^7\text{Be}(e^-, \nu)^7\text{Li}$. This process requires high temperatures ($> 10^7$ K) for the first reaction to occur and fast mixing (such as convection) to transport the by-products to a cool region of the star ($< 3 \times 10^6$ K) for lithium to be long-lived. These conditions are met at the base of the convection zones in luminous asymptotic giant branch (AGB) stars. How-

ever, understanding Li-rich stars¹ found along the red giant branch (RGB) presents a problem because these stars' convection zones are too cool to synthesize ^7Be . Thus, the ^3He reaction must occur below the convection zone, and a fast non-convective mixing mechanism is required to connect the convection zone to the deeper layers of the star in order to explain the enriched surface abundances.

Through a series of observations and advances in evolution modeling (e.g., Charbonnel & Balachandran 2000, Denissenkov & Vandenberg 2003, Eggleton et al. 2008), it has become largely accepted that red giants evolving through the luminosity bump stage of evolution likely experience a short-lived phase of enriched Li. A number of deep mixing mechanisms for this stage of evolution have been proposed, including ther-

¹ Unless otherwise stated, “Li-rich” in this paper refers to a RG whose $A(\text{Li})$ meets or exceeds the commonly used threshold of 1.5 dex.

mohaline mixing (Charbonnel & Zahn 2007), magnetic buoyancy (Busso et al. 2007), and the hybrid magneto-thermohaline mixing (Denissenkov et al. 2009). However, as the number of the relatively rare Li-rich stars continues to grow, it has become clear that they are not restricted to just the luminosity bump and AGB, but instead are found along the RGB. A new short-lived phase of Li-richness was hypothesized by Kumar et al. (2011, hereafter K11), who suggested that Li might be regenerated during the He-flash. This mechanism would account for the population of Li-rich red giants with temperatures too warm to be luminosity bump stars and that fall in a narrow luminosity range that coincides with the red clump (RC). This He-flash phenomenon would be relevant for stars in a narrow mass range of $\sim 1.5\text{--}2.25 M_{\odot}$ (K11), the upper limit being defined by the maximum mass that experiences a He flash, and the lower limit by the stars that maintain a relatively large reservoir of ${}^3\text{He}$. For the upper bound, Cassisi et al. (2016) showed that the transition occurs closer to $1.8\text{--}1.9 M_{\odot}$. At least one Li-rich star is known to be in this mass range and is confirmed to be a He-burning star via asteroseismology (Silva-Aguirre et al. 2014).

As a test of the hypothesis suggested by K11, we observed RC stars in four open clusters with ages and metallicities that place their RC stars in the mass range specified by K11. In three of the four clusters, we also observed RGs at other evolutionary stages to constrain the pre-He flash abundances. In addition to $A(\text{Li})$, we also measure ${}^{12}\text{C}/{}^{13}\text{C}$. Many of the Li-rich field stars in K11 have ${}^{12}\text{C}/{}^{13}\text{C}$ that is much lower than predicted from standard evolution models, presumably a consequence of the same mixing that brought the synthesized Li into the convection zone. Although newly synthesized Li can be destroyed if exposed to high enough temperatures, the altered ${}^{12}\text{C}/{}^{13}\text{C}$ will persist as evidence of the past deep mixing.

The selection and observation of the stars in this study are described in Sections 2 and 3, respectively. In Section 4, we outline the measurement of Li abundances and ${}^{12}\text{C}/{}^{13}\text{C}$. In Section 5, we present the significance of our results, and we give our conclusions in Section 6.

2. CLUSTER SELECTION

The four clusters in this study (Collinder 110, NGC 2204, NGC 2506, and NGC 6583) were selected so that the RC stars fell within the mass range of $1.5\text{--}2.25 M_{\odot}$, based on the predictions in K11. Table 1 lists the adopted cluster parameters (age, dereddened distance modulus, reddening, and metallicity) that were used to select the four clusters for study. We used Bressan et al. (2012) isochrones to estimate the initial masses of the stars currently at the RC stage in each cluster, and our sample spans $1.6\text{--}2.2 M_{\odot}$. Because of

uncertainties in the cluster parameters, some of the true masses may fall outside of the narrow mass range we wish to probe.

Table 1. Literature Cluster Parameters

Cluster	Age (Gyr)	$(m - M)_0$ (mag)	$E(B - V)$	[Fe/H] (dex)	M_{RC} (M_{\odot})
Collinder 110	1.7 ^c	11.82 ^a	0.38 ^b	+0.03 ^c	1.9
NGC 2204 ^d	2.0	13.06	0.08	-0.23	1.6
NGC 2506 ^e	1.99	12.53	0.04	-0.41	1.6
NGC 6583 ^f	1.0	11.55	0.51 ^g	+0.37 ^h	2.2

^a From WEBDA and within the range of Bragaglia & Tosi (2003).

^b Bragaglia & Tosi (2003)

^c Pancino et al. (2010)

^d Jacobson et al. (2011)

^e Mermilliod & Mayor (2007)

^f Carraro et al. (2005)

^g from $V - I = 0.63$, using $E(V - I)/E(B - V) = 1.244$

^h Magrini et al. (2010)

Individual stars for each cluster were selected using color-magnitude diagrams (CMDs), as illustrated in Figure 1. The photometric data were downloaded from the WEBDA database², and the photometric sources for each cluster can be found in Tables 2–5. The black dots represent all of the stars in the respective photometric sources, and the large symbols represent stars observed for this study. Candidate RC stars are identified by circles, and RGs at other evolutionary stages are represented by squares. (The meaning for the different symbol colors/shading will be described later.) Cluster isochrones (Bressan et al. 2012) adopting ages from Table 1 and metallicities derived in Section 4.2 are also plotted. The age of NGC 6583 is such that the red giants are at the upper edge of the critical mass range defined by K11 and higher than the upper bound suggested by Cassisi et al. (2016), which accounts for the lack of the luminosity bump feature in the isochrone.

3. OBSERVATIONS

All of the observations for this project were carried out with the Magellan Inamori Kyocera Echelle (MIKE) spectrograph on the Clay 6.5 m telescope at Las Campanas Observatory. Depending on the night’s seeing conditions and other projects being observed, we used

² <https://www.univie.ac.at/webda/>

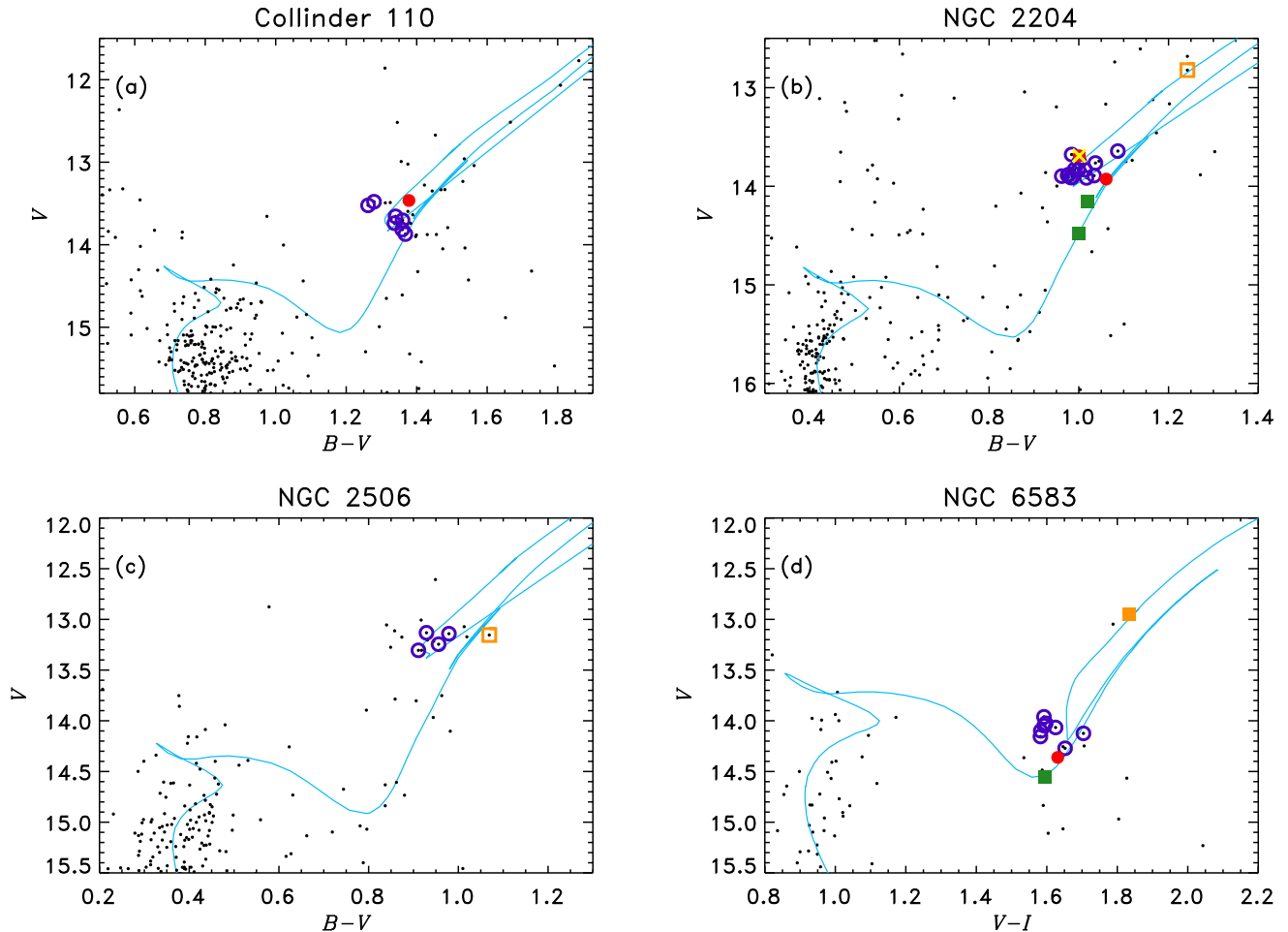


Figure 1. Color–magnitude diagrams of the four open clusters in this study. The isochrones are from [Bressan et al. \(2012\)](#) and adopt the properties given in Table 1 except for cluster metallicity, which comes from our calculated values in Section 4.2. The black dots represent all candidate cluster stars, whereas large symbols denote stars analyzed in this study. RC candidate stars are circles, with the red, filled circles indicating stars with high Li (all stars with $A(\text{Li}) > 1.5$ dex and two stars in NGC 2204 that are just below this cut-off but have $A(\text{Li})$ higher than most of the other stars in the cluster) and the purple, open circles indicating stars with low Li. Squares represent stars selected to be comparison stars: green are lower RGB stars and orange are upper RGB stars. Filled squares have high Li, while open squares have low Li. The yellow \times in NGC 2204 is a known single-lined spectroscopic binary.

either the $0.5''$ slit or the $0.7''$ slit, which yields resolving powers of $\sim 44,000$ and $31,000$, respectively. On each night, we also observed 2–3 radial velocity (RV) standard stars. We observed a Th–Ar spectrum with each pointing toward a field star or cluster. Additional Th–Ar spectra were taken approximately every 30 minutes during extended pointings toward a given cluster. To reduce the data, we used the Carnegie python pipeline ([Kelson 2003](#)).³ The pipeline first performs standard CCD processing tasks, such as overscan subtraction, bad pixel masking, flat fielding, and sky subtraction on the stellar spectra and calibration spectra. It extracts both a sky spectrum and stellar spectrum from each target star ob-

servation and wavelength calibrates these spectra with the Th–Ar lamp spectra. All of the echelle orders from the red arm of the spectrograph, spanning $4800\text{--}9400 \text{ \AA}$, were combined to a one-dimensional format. After measuring the RV (Section 4.1), the spectra were velocity shifted to the stellar rest frame.

Tables 2–5 list the red giants observed in each cluster. Nine stars were observed in Collinder 110 (Table 2) using the $0.5''$ slit, and all of these stars are RC candidates. Nineteen stars were observed in NGC 2204 (Table 3) using the $0.7''$ slit, of which sixteen are RC candidate stars, two are lower RGB stars, and one is near the RGB tip. One of the stars, MMU 4119, is a suspected spectroscopic binary ([Mermilliod & Mayor 2007](#)). In NGC 2506 (Table 4), only five stars were observed, of which four are RC candidates. The fifth star is

³ Available at <http://code.obs.carnegiescience.edu/mike>

near the luminosity bump of the cluster. All stars were observed with the $0.5''$ slit. Finally, eleven stars were observed in NGC 6583 (Table 5). Both slit sizes were

utilized because seeing conditions changed dramatically over the course of the night. Nine of the stars are RC candidates, one star is at the base of the RGB, and one star is on either the upper RGB or AGB.

Table 2. Observed Red Giant Candidates: Collinder 110

Star	R.A. (J2000.0)	Decl. (J2000.0)	V^a (mag)	$B - V^a$ (mag)	UT Date	t_{exp} (s)	S/N (6706 Å)	Slit ($''$)	Classification (Initial/Revised)
1134	06:38:45.0	02:04:23.5	13.70	1.36	2013 Jan 26	3600	113	0.5	RC
2119	06:38:43.3	02:02:18.2	13.52	1.26	2013 Jan 27	4200	92	0.5	RC
2129	06:38:41.1	02:01:05.3	13.66	1.34	2013 Jan 26	3240	118	0.5	RC
2223	06:39:03.5	01:59:19.8	13.48	1.28	2013 Jan 27	2820	92	0.5	RC
3122	06:38:34.7	02:01:41.0	13.46	1.38	2014 Mar 19	4050	105	0.5	RC/RGB
3144	06:38:30.3	02:03:03.0	13.49	1.31	2014 Mar 20	2000	78	0.5	RC
3244	06:38:16.0	02:02:24.3	13.74	1.34	2013 Jan 26	2640	104	0.5	RC
4260	06:38:32.3	02:07:24.7	13.87	1.37	2013 Jan 27	2400	77	0.5	RC
5125	06:38:40.2	02:01:38.5	13.82	1.36	2013 Jan 27	3200	83	0.5	RC

^a [Bragaglia & Tosi \(2003\)](#)

Table 3. Observed Red Giant Candidates: NGC 2204

Star	R.A. (J2000.0)	Decl. (J2000.0)	V^a (mag)	$B - V^a$ (mag)	UT Date	t_{exp} (s)	S/N (6706 Å)	Slit ($''$)	Classification (Initial/Revised)
1124	06:15:29.0	-18:39:09.8	13.84	1.00	2014 Jan 06	1800	94	0.7	RC
1212	06:15:20.1	-18:37:57.8	13.88	0.98	2014 Jan 07	1800	121	0.7	RC
1330	06:15:26.7	-18:33:25.1	13.76	1.04	2014 Jan 07	1400	113	0.7	RC
2212	06:15:49.7	-18:37:39.4	12.82	1.24	2014 Jan 06	800	122	0.7	AGB
2229	06:15:36.9	-18:36:08.9	13.83	1.01	2014 Jan 07	1400	106	0.7	RC
2311	06:16:02.1	-18:38:46.5	13.64	1.09	2014 Jan 07	1200	109	0.7	RC
2330	06:15:34.4	-18:35:03.1	14.48	1.00	2014 Jan 07	2600	114	0.7	RGB
3205	06:15:46.0	-18:40:44.0	13.91	0.98	2014 Jan 07	1400	109	0.7	RC
3215	06:15:45.3	-18:43:34.9	13.75	1.00	2014 Jan 06	1400	114	0.7	RC
3321	06:15:43.3	-18:46:20.1	13.83	0.99	2014 Jan 06	2000	116	0.7	RC
4115	06:15:27.9	-18:40:34.0	14.15	1.02	2014 Jan 07	1680	108	0.7	RGB
4116	06:15:27.5	-18:40:13.9	13.93	1.06	2014 Jan 06	1600	117	0.7	RC/RGB
4119	06:15:27.2	-18:40:44.3	13.69	1.00	2014 Jan 07	1200	104	0.7	RC/RGB ^b
4211	06:15:13.6	-18:41:49.3	13.68	0.98	2014 Jan 06	1200	103	0.7	RC
4223	06:15:32.9	-18:43:11.9	13.89	1.03	2014 Jan 06	1840	113	0.7	RC
4303	06:15:03.9	-18:41:07.6	13.90	0.96	2014 Jan 06	1400	100	0.7	RC
5352	06:15:50.8	-18:34:19.4	13.91	1.02	2014 Jan 06	1800	102	0.7	RC
5980	06:15:33.7	-18:42:12.1	13.89	0.98	2014 Jan 06	1800	112	0.7	RC
6330	06:15:26.1	-18:31:48.8	13.91	0.98	2014 Jan 06	1800	114	0.7	RC

^a [Kassisi et al. \(1997\)](#)

^b Suspected binary

Table 4. Observed Red Giant Candidates: NGC 2506

Star	R.A. (J2000.0)	Decl. (J2000.0)	V^a (mag)	$B - V^a$ (mag)	UT Date	t_{exp} (s)	S/N (6706 Å)	Slit ($''$)	Classification (Initial/Revised)
2380	08:00:09.2	-10:49:09.0	13.14	0.98	2013 Jan 27	1680	68	0.5	RC
3265	07:59:50.8	-10:46:40.0	13.15	1.07	2013 Jan 27	1320	52	0.5	RGB/RC? ^b
4138	08:00:01.4	-10:45:39.3	13.31	0.91	2013 Jan 27	2220	78	0.5	RC
4205	07:59:51.3	-10:46:17.4	13.24	0.96	2013 Jan 26	1680	96	0.5	RC
4240	07:59:52.6	-10:44:50.0	13.13	0.93	2013 Jan 26	1620	94	0.5	RC

^a Kim et al. (2001)^b Suspected binary**Table 5.** Observed Red Giant Candidates: NGC 6583

Star	R.A. (J2000.0)	Decl. (J2000.0)	V^a (mag)	$V - I^a$ (mag)	UT Date	t_{exp} (s)	S/N (6706 Å)	Slit ($''$)	Classification (Initial/Revised)
10	18:15:51.1	-22:07:15.2	12.94	1.84	2014 Jun 19	840	112	0.5	AGB/RGB
33	18:15:52.6	-22:09:53.2	14.02	1.60	2014 Jun 19	2280	109	0.5	RC
34	18:15:43.9	-22:09:00.9	13.96	1.59	2014 Jun 19	1920	100	0.5	RC
38	18:15:48.2	-22:09:53.2	14.05	1.59	2014 Jun 19	1600	129	0.7	RC
39	18:15:56.6	-22:07:32.4	14.07	1.62	2014 Jun 19	1800	119	0.7	RC
42	18:15:50.2	-22:09:55.5	14.12	1.70	2014 Jun 19	900	70	0.7	RC
46	18:15:51.2	-22:07:26.6	14.10	1.58	2014 Jun 19	2400	96	0.5	RC
50	18:15:48.3	-22:09:33.5	14.15	1.58	2014 Jun 19	1800	106	0.7	RC/RGB?
62	18:15:51.2	-22:08:28.1	14.27	1.65	2014 Jun 19	2000	109	0.7	RC
72	18:15:54.3	-22:08:05.7	14.36	1.63	2014 Jun 19	2200	98	0.7	RC/RGB?
92	18:15:51.7	-22:08:30.6	14.55	1.60	2014 Jun 19	3800	107	0.5	RGB

^a Carraro et al. (2005)

4. STELLAR CHARACTERIZATION

4.1. Radial Velocities

Heliocentric radial velocities (v_{helio}) were measured for each star by cross-correlating the 1D spectra with the high-resolution Arcturus atlas spectrum (Hinkle et al. 2000) with the IRAF procedure *fxcor*. The spectra were also cross-correlated with the Hinkle et al. (2000) telluric spectrum in the wavelength ranges of 6475–6675 Å, 6980–7060 Å, and 7850–8125 Å to measure slit centering errors, since the seeing disk was at times smaller than the slit width. We found RV offsets in the telluric line centers as high as 2.4 km s⁻¹. The final v_{helio} measurements reported here are $v_{\text{helio}} = v_{\text{stellar}} + v_{\text{cor}} - v_{\text{telluric}}$, where v_{stellar} is the relative RV of the object spectra with respect to the Arcturus spectrum (which is in the stellar rest frame), v_{cor} is the heliocentric RV correction, and v_{telluric} is the relative RVs of the telluric lines

in the observed spectra with respect to the atlas telluric spectrum. Using the corrections from the telluric line cross-correlation better reproduced the v_{helio} of the RV standard stars that we observed.

The average cluster velocities were calculated using an iterative sigma-clipping algorithm, clipping at 3σ . The results are given in Table 6, along with literature measurements. Two stars in NGC 2204 were clipped: 2330 with $v_{\text{helio}} = 96.5$ km s⁻¹ and 4119 with $v_{\text{helio}} = 76.8$ km s⁻¹. The latter is a suspected spectroscopic binary star that is still a cluster member (Mermilliod & Mayor 2007). We maintain star 2330 in our analysis, but caution that it is a potential non-member based on its RV. If it is a member, it is on the lower RGB. Individual v_{helio} are listed in the final column of Table 7. The uncertainty in the v_{helio} is dominated by systematic errors. The random errors are all < 0.1 km s⁻¹ with an aver-

age 0.04 km s^{-1} . Comparing the v_{helio} of five RV standard stars (HD 107328, HD 171391, HD 66141, HD 26162, and HD 203638) measured on multiple nights

to the accepted values in “The Astronomical Almanac” (U. S. Government Printing Office 2006), we estimate a systematic uncertainty of $0.2\text{--}0.3 \text{ km s}^{-1}$.

Table 6. Comparison of Measured Open Cluster Properties

Cluster Name	v_{helio} (km s^{-1})	Lit. v_{helio} (km s^{-1})	Reference	[Fe/H] (dex)	$\sigma_{[\text{Fe}/\text{H}]}$ (dex)	Lit. [Fe/H] (dex)	Reference
Collinder 110	$+37.0 \pm 1.3$	$+41.0 \pm 3.8$	1	-0.09	0.04	+0.03	1
	...	$+38.7 \pm 0.8$	2
NGC 2204	$+91.1 \pm 1.2$	$+88.4 \pm 1.3$	3	-0.21	0.04	-0.23	3
	...	$+91.4 \pm 1.3$	4	-0.32	7
NGC 2506	$+82.4 \pm 1.1$	$+83.2 \pm 1.6$	4, 5	-0.25	0.09	-0.41	4
	-0.44	7
	-0.24	8, 9
NGC 6583	-2.3 ± 1.1	-3.0 ± 0.4	6	+0.17	0.05	+0.37	6

References—(1) Pancino et al. (2010), (2) Carlberg (2014), (3) Jacobson et al. (2011), (4) Mermilliod & Mayor (2007), (5) Mermilliod et al. (2008), (6) Magrini et al. (2010), (7) Friel et al. (2002), (8) Mikolaitis et al. (2011), (9) Lee et al. (2012)

4.2. Spectroscopic Stellar Parameters

Although it is common in open cluster studies to use photometric temperatures and isochrones to constrain surface gravities, we opted to do a full spectroscopic derivation of the stellar parameters. This provides a more homogenous determination of stellar T_{eff} and $\log g$ across our sample. We used the iron line list of Carlberg et al. (2012), which was compiled for deriving stellar parameters of red giant stars. Equivalent widths (EqWs) were all measured by hand using IRAF’s *plot* routine, using gaussian profiles and deblending when necessary. The high-resolution Arcturus atlas (Hinkle et al. 2000) was used as a template to identify blended lines. We used the 2014 version of the stellar line analysis program, MOOG⁴ (Snedden 1973), and MARCS spherical atmosphere models (Plez 2008) to compute abundances. To solve for the stellar T_{eff} , $\log g$, [Fe/H], and ξ , we used the standard requirements that there should be no trend of the output $A(\text{Fe I})$ with either the excitation potential or strength of the

iron lines and that $A(\text{Fe I})$ should equal $A(\text{Fe II})$. The 2014 version of MOOG adopts $A(\text{Fe})_{\odot} = 7.50$, while the MARCS models adopt $A(\text{Fe})_{\odot} = 7.45$. However, the difference in the atmosphere structure of two models that differ in [M/H] by 0.05 dex is too small to affect our abundances. The Carlberg et al. (2012) line list yields a slightly higher solar abundance of $A(\text{Fe})_{\odot} = 7.53$, which we adopt to translate our stellar $A(\text{Fe})$ to [Fe/H]. In Table 7, we give the results of our stellar parameter analysis and the uncertainties in each parameter. The uncertainties in ξ are the variations that arise when the slope of $A(\text{Fe I})$ vs. EqW/ λ is varied within the 1σ uncertainty of the fitted slope (Neuforge-Verheecke & Magain 1997). Similarly, the uncertainty in T_{eff} uses the uncertainty in the slope of $A(\text{Fe I})$ vs. excitation potential. It also includes the contribution from the ξ uncertainty. The uncertainties in [Fe/H] and $\log g$ are the standard deviations in the Fe I and Fe II lines, respectively. These dominate over the uncertainty arising from sensitivities to the other stellar parameters.

Table 7. Stellar Parameters

Cluster	Star	T_{eff} (K)	$\sigma_{T_{\text{eff}}}$ (K)	$\log g$ (dex)	$\sigma_{\log g}$ (dex)	[Fe/H] (dex)	$\sigma_{[\text{Fe}/\text{H}]}$ (dex)	ξ (km s^{-1})	σ_{ξ} (km s^{-1})	$v \sin i$ (km s^{-1})	$\sigma_{v \sin i}$ ^a (km s^{-1})	ζ^{b} (km s^{-1})	v_{helio} (km s^{-1})
Collinder 110	1134	4960.	62.	2.80	0.09	-0.13	0.10	1.47	0.06	1.0	0.0	4.99	+37.2
Collinder 110	2119	4970.	64.	2.80	0.14	-0.16	0.10	1.14	0.06	5.9	0.2	5.23	+35.6

Table 7 continued

⁴ available at <http://www.as.utexas.edu/~chris/moog.html>

Table 7 (*continued*)

Cluster	Star	T_{eff} (K)	$\sigma_{T_{\text{eff}}}$ (K)	$\log g$ (dex)	$\sigma_{\log g}$ (dex)	[Fe/H] (dex)	$\sigma_{[\text{Fe}/\text{H}]}$ (dex)	ξ (km s ⁻¹)	σ_{ξ} (km s ⁻¹)	$v \sin i$ (km s ⁻¹)	$\sigma_{v \sin i}$ ^a (km s ⁻¹)	ζ ^b (km s ⁻¹)	v_{helio} (km s ⁻¹)
Collinder 110	2129	4940.	59.	2.70	0.09	-0.11	0.10	1.35	0.05	1.1	0.0	4.98	+38.0
Collinder 110	2223	4990.	69.	2.80	0.07	-0.07	0.12	1.43	0.06	1.0	0.0	5.34	+36.2
Collinder 110	3122	4800.	80.	2.65	0.10	-0.10	0.13	1.33	0.07	1.0	0.0	4.81	+39.2
Collinder 110	3144	4870.	72.	2.55	0.12	-0.07	0.12	1.37	0.06	1.4	0.0	4.97	+37.2
Collinder 110	3244	4960.	62.	2.85	0.09	-0.08	0.10	1.39	0.06	1.0	0.0	4.95	+38.0
Collinder 110	4260	4980.	64.	2.75	0.13	-0.10	0.11	1.19	0.06	1.0	0.0	4.85	+36.7
Collinder 110	5125	5130.	72.	3.05	0.11	+0.00	0.12	1.45	0.07	1.0	0.0	5.39	+34.6
NGC 2204	1124	5030.	56.	2.65	0.13	-0.24	0.10	1.44	0.06	2.7	0.0	5.43	+91.2
NGC 2204	1212	5080.	55.	2.75	0.08	-0.21	0.10	1.28	0.05	2.5	0.0	5.54	+88.1
NGC 2204	1330	5120.	71.	2.85	0.10	-0.18	0.12	1.43	0.07	1.0	0.0	5.83	+88.9
NGC 2204	2212	4570.	62.	2.00	0.10	-0.27	0.10	1.55	0.05	1.9	0.0	5.21	+91.7
NGC 2204	2229	5060.	52.	2.70	0.14	-0.18	0.09	1.35	0.05	1.5	0.0	5.54	+91.3
NGC 2204	2311	4950.	61.	2.55	0.13	-0.26	0.11	1.46	0.06	1.5	0.0	5.40	+91.8
NGC 2204	2330	5080.	59.	3.15	0.10	-0.17	0.10	1.23	0.06	1.0	0.0	4.83	+96.5
NGC 2204	3205	5070.	72.	2.85	0.07	-0.21	0.12	1.38	0.07	1.0	0.0	5.47	+93.3
NGC 2204	3215	5010.	61.	2.75	0.06	-0.17	0.10	1.42	0.06	1.0	0.0	5.45	+91.5
NGC 2204	3321	5100.	58.	2.80	0.11	-0.15	0.10	1.32	0.06	2.3	0.0	5.67	+91.3
NGC 2204	4115	4880.	63.	2.70	0.09	-0.21	0.10	1.28	0.06	2.2	0.0	4.62	+91.5
NGC 2204	4116	4860.	63.	2.65	0.11	-0.26	0.11	1.35	0.06	1.0	0.0	4.80	+92.9
NGC 2204	4119	4820.	71.	2.65	0.14	-0.24	0.11	1.27	0.06	1.0	0.0	4.96	+76.8
NGC 2204	4211	5030.	65.	2.70	0.10	-0.19	0.11	1.41	0.06	1.0	0.0	5.63	+90.7
NGC 2204	4223	5260.	101.	3.06	0.11	-0.15	0.17	1.62	0.10	1.3	0.0	6.15	+91.0
NGC 2204	4303	5010.	71.	2.60	0.10	-0.26	0.12	1.47	0.07	1.0	0.0	5.27	+91.3
NGC 2204	5352	5010.	68.	2.80	0.09	-0.15	0.11	1.36	0.06	1.0	0.0	5.25	+90.6
NGC 2204	5980	5050.	63.	2.70	0.10	-0.23	0.11	1.46	0.06	1.8	0.0	5.43	+91.0
NGC 2204	6330	5000.	63.	2.70	0.06	-0.25	0.11	1.42	0.06	1.0	0.0	5.22	+90.9
NGC 2506	2380	4980.	65.	2.55	0.09	-0.32	0.11	1.45	0.06	1.0	0.0	5.31	+82.8
NGC 2506	3265	5250.	100.	3.05	0.15	-0.10	0.17	1.52	0.10	1.0	0.0	6.24	+80.3
NGC 2506	4138	5030.	64.	2.70	0.09	-0.29	0.11	1.45	0.06	1.0	0.0	5.27	+82.9
NGC 2506	4205	5050.	61.	2.80	0.08	-0.25	0.10	1.41	0.06	1.0	0.0	5.42	+83.7
NGC 2506	4240	5000.	66.	2.70	0.09	-0.27	0.11	1.43	0.06	1.0	0.0	5.38	+82.4
NGC 6583	10	4350.	103.	2.10	0.28	+0.05	0.15	1.61	0.09	2.3	0.6	4.26	0.0
NGC 6583	33	4870.	81.	2.80	0.12	+0.19	0.13	1.60	0.07	1.5	0.0	4.54	-3.2
NGC 6583	34	4860.	73.	2.65	0.11	+0.16	0.12	1.60	0.06	1.9	0.0	4.58	-2.7
NGC 6583	38	4900.	75.	2.75	0.16	+0.18	0.12	1.54	0.07	2.1	0.0	4.59	-1.7
NGC 6583	39	4830.	76.	2.50	0.12	+0.15	0.12	1.64	0.06	5.0	0.0	4.38	-1.0
NGC 6583	42	4840.	90.	2.60	0.23	+0.18	0.14	1.68	0.08	3.3	0.0	4.36	-2.5
NGC 6583	46	4910.	77.	2.80	0.13	+0.17	0.12	1.56	0.07	1.5	0.0	4.56	-2.5
NGC 6583	50	4970.	85.	3.00	0.16	+0.27	0.13	1.64	0.08	2.5	0.0	4.67	-2.8
NGC 6583	62	4910.	84.	2.80	0.15	+0.20	0.13	1.61	0.07	2.0	0.0	4.39	-1.8
NGC 6583	72	4940.	92.	2.95	0.16	+0.16	0.14	1.55	0.08	5.0	0.2	4.37	-2.7
NGC 6583	92	4980.	71.	2.95	0.14	+0.19	0.11	1.42	0.06	1.1	0.0	4.28	-4.1

^a Values of 0.0 refer to upper limits.

^b Adopted

In Figure 2, we find overall good agreement between our derived T_{eff} and $\log g$ and the values predicted from isochrones. However, the classification of objects as ei-

ther candidate RC stars (circles) or candidate non-RC stars (squares) from the photometry (Figure 1) do not necessarily persist when plotted in this phase space. Our

RC stars tend to scatter along a diagonal line in $T_{\text{eff}} - \log g$ but at a given temperature, the clump and first ascent stars appear to cleanly separate in $\log g$, as is especially apparent in NGC 2204. In that cluster, two of the RC candidate stars appear to be first ascent stars just below the luminosity bump. The same is true of one of the RC candidates in Collinder 110. These stars have revised classifications of ‘RGB’ in Tables 2 and 3. All of the clump candidates in NGC 2506 appear to be bona fide RC stars. The picture in NGC 6583 is still murky. The two hottest RC candidates may be first ascent stars, and their revised classifications in Table 5 is ‘RGB?.’ In the discussion that follows, ‘candidate RC’ stars refers to the stars that have initial classifications of ‘RC;’ their revised classification may be different.

Comparing Figures 1 and 2, we were surprised to find that the single non-RC star that we observed in NGC 2506 has the hottest spectroscopic temperature (5250 K), even though it has the reddest $B - V$ of the stars we observed. Our spectroscopic measurements place NGC 2506 3265 somewhat off of the isochrone, but we note that this star has the lowest signal-to-noise ratio (S/N) in our entire sample (only 68). Using the color–temperature relations of Ramírez & Meléndez (2005), the $(B - V)_0$ color yields $T_{\text{eff}} = 4690$ K. To test the source of this discrepancy, we computed color–temperatures from two independent photometric sources in the literature. Optical $(V - I)_0$ photometry from Lee et al. (2012) yields a hotter temperature of $T_{\text{eff}} = 4820$ K, while 2MASS $(J - K)_0$ (using Houdashelt et al. 2000 color transformation) yields an even higher $T_{\text{eff}} = 5050$ K. This latter value is most consistent with the spectroscopic temperature but is still 200 K cooler. All of the literature photometry of NGC 2506 3265 is consistent with the RC and bump magnitude of the isochrones. The optical colors correspond to the luminosity bump, while the infrared color prefers the RC. Thus, this star’s evolutionary stage remains ambiguous. It is also possible that the star is a non-member considering that both its v_{helio} and $[\text{Fe}/\text{H}]$ appear to be deviant, although neither parameter is sufficiently deviant compared to the errors to confidently confirm its non-membership. Comparing our v_{helio} measurement ($80.3 \pm 0.3 \text{ km s}^{-1}$) to the literature suggests that the star may in fact be a binary. Carlberg (2014) finds 83.7 ± 1.4 while Mermilliod & Mayor (2007) find $85.33 \pm 0.46 \text{ km s}^{-1}$.

4.2.1. $[\text{Fe}/\text{H}]$ and Equivalent Width Comparison

In Table 6 and Figure 3, we compare our average cluster metallicities to those in the literature. Most of the literature sources are those listed in Table 1. For the two most metal-poor clusters, we get excellent agreement with at least one literature source, although other

literature sources disagree outside the uncertainties. For the more metal-rich clusters, we find lower metallicities than the literature studies do. To test whether the cause of this discrepancy arises from our stellar parameter derivation, we also compute the metallicities using the same EqW measurements but using T_{eff} derived from the dereddened colors and magnitudes of the stars and $\log g$ derived from the stellar masses estimated from the isochrones. The bottom panel of Figure 3 shows that comparison. The photometric cluster metallicities are in good agreement with the spectroscopic ones but are systematically lower.

Another possible cause of the discrepancy may be in the EqW measurements. The presence of many, weak unresolved metal lines could lead to systematic differences in the continuum placement. Fortunately, there are two stars each in Collinder 110 and NGC 6583 with literature EqW abundances. Pancino et al. (2010) measured abundances of Collinder 110 stars 2129 and 3144, and there are 29 iron lines overlapping our studies. Similarly, Magrini et al. (2010) measured abundances of the NGC 6583 stars 46 and 62 with 22 lines overlapping our studies. Figure 4 shows that our measurements agree quite well, and there is no systematic underestimation of EqWs in this study. The mean and standard deviation of ΔEqW are similar in size to that attained by Pancino et al. (2010), when they compared their results to earlier studies.

4.3. Rotational Velocities

The projected rotational velocities ($v \sin i$) were measured by fitting the profiles of up to six relatively isolated Fe lines in our line list (5307.36, 5638.26, 5855.08, 6151.62, 6165.36, and 6750.15 Å). In addition to the rotation, there are two other major sources of broadening that must be accounted for: the line spread function (or instrumental broadening) and the macroturbulent broadening (ζ). The former can be measured from the Th–Ar lines appearing in the same echelle order as the Fe lines. Discriminating uniquely between $v \sin i$ from ζ is difficult (if not impossible) at the spectral resolution and S/N of our data. Instead, we estimate ζ using previously defined relationships between ζ and other standard stellar parameters. We tested two different prescriptions: the $\zeta(T_{\text{eff}}, \text{LC})$ relationships of Hekker & Meléndez (2007), where ‘LC’ refers to the luminosity class, and the $\zeta(\log T_{\text{eff}}, \log L/L_{\odot})$ relationships of Massarotti et al. (2008). The former prescription tended to give larger ζ by ~ 0.5 – 2.5 km s^{-1} compared to the latter. We adopted the Massarotti et al. (2008) prescription since we have fairly accurate luminosities for our stars. We then generated synthetic spectra of varying $v \sin i$ for each of the six spectra lines, and used a χ^2 minimization to select the best $v \sin i$.

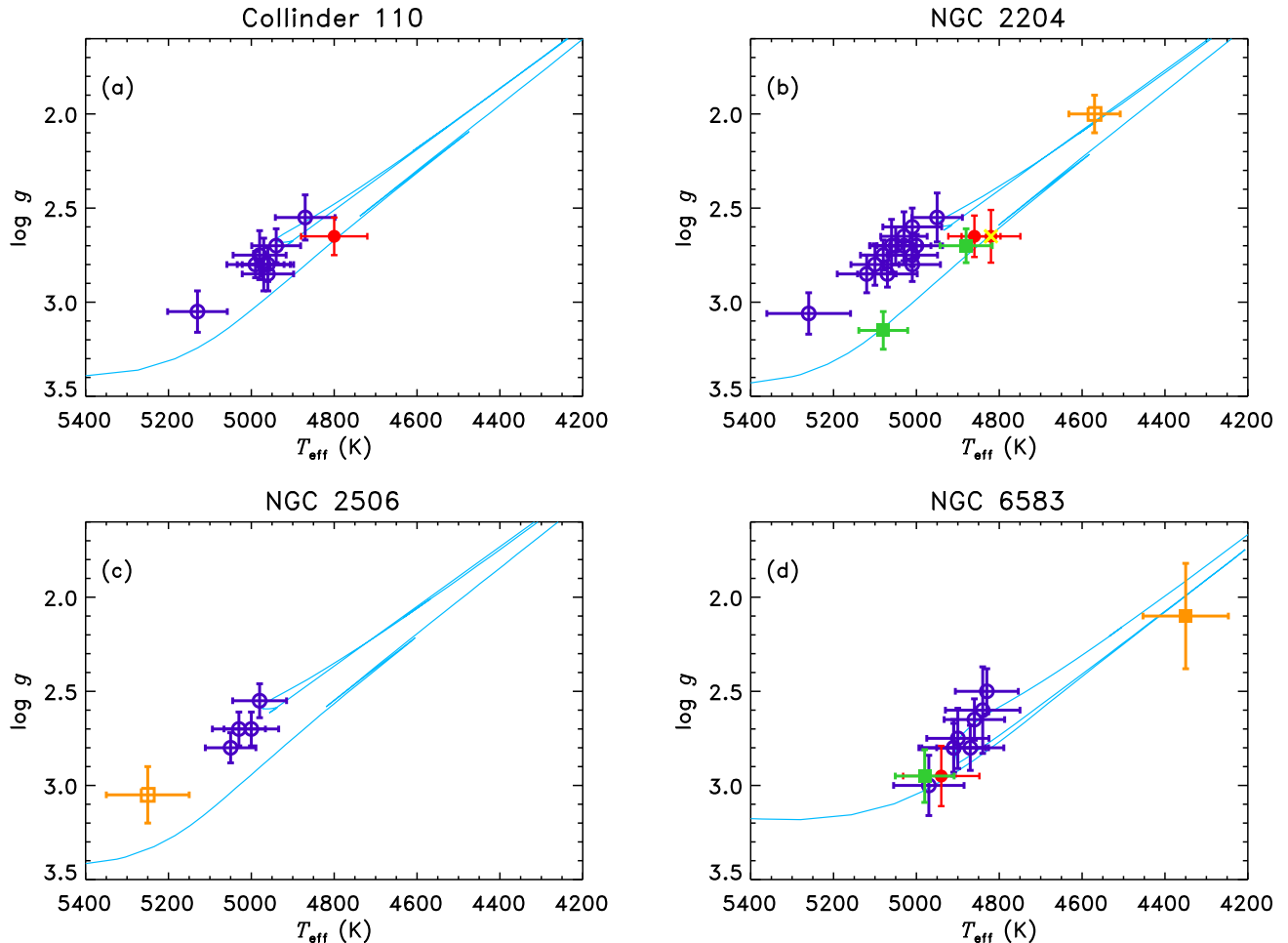


Figure 2. $T_{\text{eff}}\text{-log } g$ diagrams of the four open clusters in this study together with their respective isochrones. The symbols are the same as in Figure 1.

The results of the broadening analysis ($v \sin i$, $\sigma_{v \sin i}$, and ζ) are given in columns 11–13 of Table 7. The majority of the RGs in this study are very slow rotators, where the instrumental and macroturbulent broadening fully account for the line profile, and in some cases over accounts for it. Upper limits are provided for these stars, which are indicated with $\sigma_{v \sin i} = 0.0 \text{ km s}^{-1}$. Only three stars have $v \sin i$ that are not upper limits. The star with the largest rotation, Collinder 110 2119, has $v \sin i = 5.9 \pm 0.3 \text{ km s}^{-1}$. Its $v \sin i$ was also measured by Carlberg (2014) via cross-correlation using high-resolution, low S/N data and was found to be $6.3 \pm 0.8 \text{ km s}^{-1}$, consistent with this result. The remaining Collinder 110 stars overlapping that study were all upper limits consistent with what is found here.

4.4. Lithium

$A(\text{Li})$ were measured by fitting spectra synthesized with MOOG to the observed data between 6706.7 and 6708.4 Å using the line list from Ghezzi et al. (2009). The spectra were fit by hand, making small adjustments

to the overall continuum level, velocity scale, and broadening to get a good match between the observed and synthetic spectra. The Li I resonance lines are blended with a Fe I line and CN lines at the resolution of our spectra. We made adjustments to the abundances of these elements first before adjusting $A(\text{Li})$. Our synthesis fits assume local thermodynamic equilibrium (LTE), and we correct for NLTE effects by interpolating the grid of Lind et al. (2009) corrections to each stars’ observed parameters.

The results of the synthesis fitting are given in Table 8. The EqW of the Li feature corresponding to the synthesis measurement or limit is also provided in the table. For some spectra, the “best fit” was still not a great match to the data, and we therefore provide a reliability parameter to flag the cases where the fits were more uncertain. As an example, NGC 2506 is the most metal-poor cluster in the sample and, because of observing conditions, the average S/N achieved for these stars is lower than all of the other clusters. Therefore, the spectra had both the weakest features to fit and the

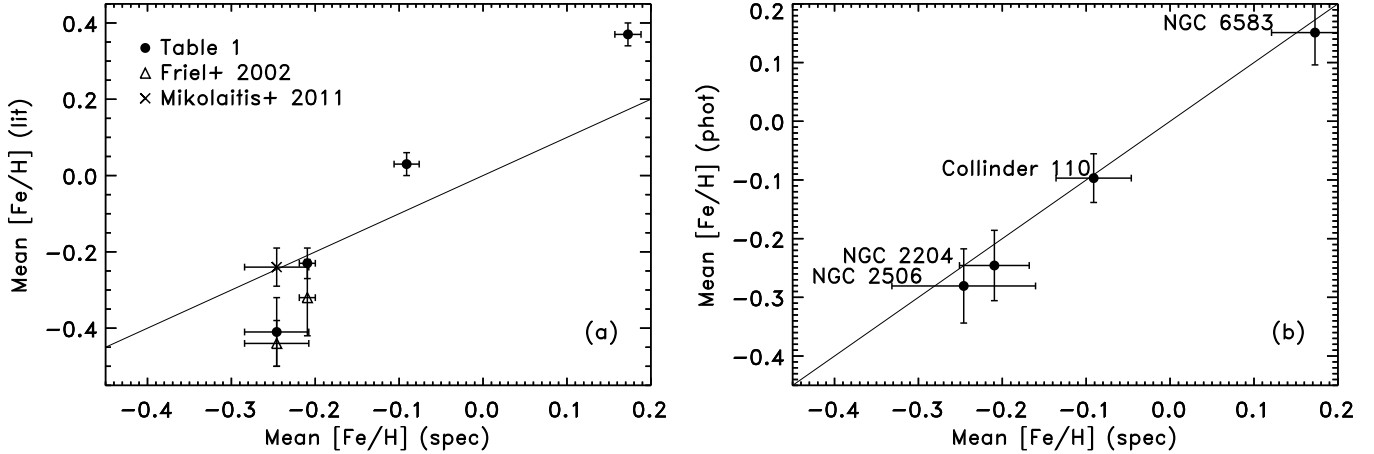


Figure 3. Comparison between our average cluster [Fe/H] and measurements from the literature (a). Comparison between the average [Fe/H] measurements from the full spectroscopic determination and from one that uses T_{eff} and $\log g$ from the photometry (b).

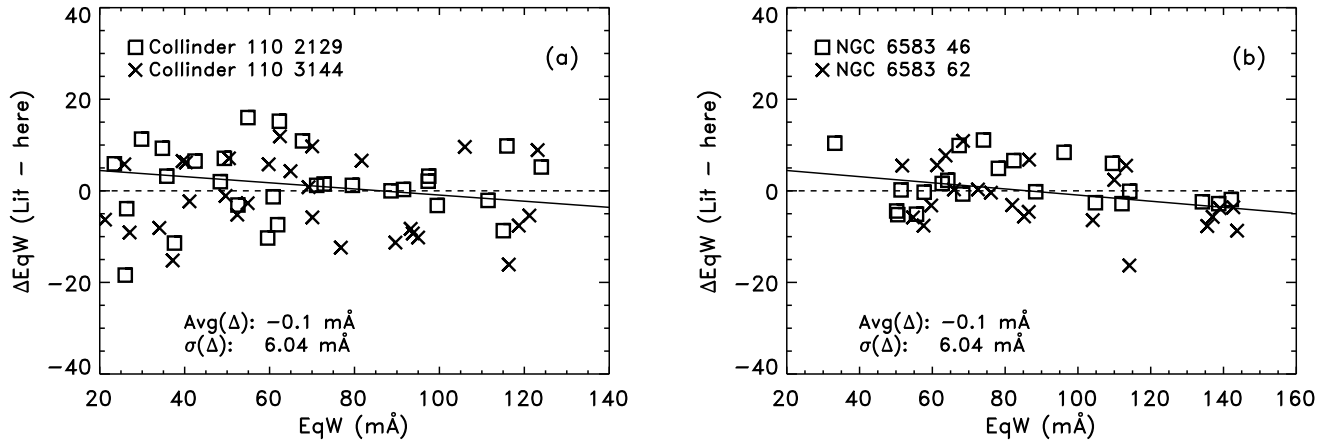


Figure 4. Comparison of our iron line equivalent width measurements to literature measurements for stars in Collinder 110 (a, [Pancino et al. 2010](#)) and NGC 6583 (b, [Magrini et al. 2010](#)). The solid lines show linear fits to the data, while the dashed lines denote the ideal case of $\Delta = 0$. The mean and standard deviation of ΔEqW is also shown on the plot.

largest noise. The stars with a quality parameter of ‘A’ are good fits, whereas ‘B’ indicates more uncertain fits.

4.5. $^{12}\text{C}/^{13}\text{C}$

The $^{12}\text{C}/^{13}\text{C}$ ratio was measured by fitting the spectral region between 8001 and 8006 Å, containing four ^{12}CN features (one blended with an Fe I line) and one ^{13}CN feature. We used the line list from [Carlberg et al. \(2012\)](#) to generate synthetic spectra. A linear correction to the continuum is fit, and the observed spectrum is cross-correlated with the synthetic spectrum to correct for small mismatches between the velocity scales. We keep the ratio of C/N fixed at 1.5 but allow the total abundance of the two elements to vary to fit the ^{12}CN features. Then we vary the $^{12}\text{C}/^{13}\text{C}$ to find the best fit to the ^{13}CN features. Telluric features are abundant in

this part of the spectrum. In most cases the telluric lines are weak, and we account for their presence by adding in their contribution using the [Hinkle et al. \(2000\)](#) atlas telluric spectrum, broadened to our instrumental resolution and scaled to fit the depth of the features.

There is one strong telluric feature near 8007.5 Å that caused significant problems. NGC 2204 was observed at an unfortunate RV that placed the ^{13}CN lines at nearly the same wavelength as this strong feature. For NGC 2506, the blue wing of this strong telluric feature is blended with the ^{13}CN line. For the stars in these two clusters, we corrected the spectra using the telluric standard stars that were observed on each night. These standards were observed at airmasses that bracketed the airmass of the cluster stars. We divided each of the cluster stellar spectra with the hot star spectrum that

was closest in airmass, adjusting the velocity and overall scaling of the hot star spectrum to get the cleanest division. In seven cases, the $^{13}\text{C/N}$ feature was not recoverable. For the NGC 2204 stars where the feature was recovered, it should be noted that the telluric feature was always stronger than the underlying stellar feature, and uncertainties in the telluric division may be large. Therefore, all of the $^{12}\text{C}/^{13}\text{C}$ measurements for

NGC 2204 should be used with caution. The results of the $^{12}\text{C}/^{13}\text{C}$ analysis are given in Table 8, which includes a quality parameter. Stars with measurements have a quality parameter ranging from ‘A’ through ‘D,’ which corresponds to decreasing quality of the fits. Those with quality of ‘X’ indicates that $^{12}\text{C}/^{13}\text{C}$ was not measurable. The two lowest quality measurements (‘D’ and ‘X’) apply only to the stars that had the hot star correction to the telluric features.

Table 8. Stellar Abundances

Cluster	Star	EqW (mÅ)	$A(\text{Li})$ (dex)	$A(\text{Li})_{\text{NLTE}}$ (dex)	$\sigma_{A(\text{Li})}^{\text{a}}$ (dex)	Quality	$^{12}\text{C}/^{13}\text{C}$	$\sigma_{^{12}\text{C}/^{13}\text{C}}^{\text{b}}$	Quality
Collinder 110	1134	8.7	0.62	0.79	0.15	A	17	5	A
Collinder 110	2119	9.7	0.68	0.84	0.16	A	22	5	B
Collinder 110	2129	4.8	0.34	0.51	0.00	A	12	5	A
Collinder 110	2223	2.9	0.18	0.34	0.00	A	15	5	C
Collinder 110	3122	63.7	1.34	1.54	0.22	A	18	5	B
Collinder 110	3144	13.0	0.68	0.88	0.00	B	10	5	C
Collinder 110	3244	6.9	0.52	0.69	0.15	A	16	5	B
Collinder 110	4260	4.0	0.30	0.47	0.00	A	17	5	B
Collinder 110	5125	3.8	0.45	0.58	0.00	A	20	5	B
NGC 2204	1124	3.7	0.31	0.46	0.00	B	X
NGC 2204	1212	5.9	0.59	0.73	0.13	A	X
NGC 2204	1330	1.7	0.07	0.20	0.00	A	16	5	D
NGC 2204	2212	0.3	-1.22	-0.95	0.00	A	12	5	D
NGC 2204	2229	4.8	0.47	0.62	0.00	B	12	5	D
NGC 2204	2311	3.6	0.19	0.36	0.00	A	12	5	C
NGC 2204	2330	35.6	1.40	1.52	0.14	A	12	5	C
NGC 2204	3205	3.9	0.39	0.53	0.17	A	X
NGC 2204	3215	7.4	0.59	0.75	0.15	B	8	5	D
NGC 2204	3321	8.3	0.75	0.89	0.13	A	9	5	D
NGC 2204	4115	50.8	1.33	1.50	0.16	A	27	5	C
NGC 2204	4116	43.7	1.23	1.40	0.16	A	X
NGC 2204	4119	46.7	1.21	1.39	0.19	A	16	5	C
NGC 2204	4211	5.6	0.49	0.64	0.16	A	X
NGC 2204	4223	1.1	0.10	0.21	0.00	A	15	5	D
NGC 2204	4303	2.2	0.09	0.24	0.00	B	10	5	D
NGC 2204	5352	17.9	1.00	1.15	0.17	B	X
NGC 2204	5980	2.1	0.12	0.27	0.00	B	18	0	D
NGC 2204	6330	7.9	0.62	0.77	0.15	B	13	5	D
NGC 2506	2380	5.6	0.43	0.59	0.00	B	X
NGC 2506	3265	9.8	1.00	1.11	0.00	B	21	5	B
NGC 2506	4138	10.1	0.76	0.90	0.15	B	10	0	C
NGC 2506	4205	5.4	0.50	0.64	0.14	B	10	5	D
NGC 2506	4240	5.8	0.48	0.63	0.00	B	9	5	C
NGC 6583	10	262.3	1.49	1.74	0.33	A	24	5	A
NGC 6583	33	20.2	0.88	1.07	0.22	A	21	5	A
NGC 6583	34	21.3	0.89	1.09	0.20	B	23	5	A
NGC 6583	38	31.9	1.13	1.32	0.20	A	22	5	A
NGC 6583	39	2.6	-0.09	0.13	0.00	A	21	5	A
NGC 6583	42	22.1	0.88	1.09	0.00	B	19	5	A
NGC 6583	46	13.8	0.76	0.94	0.20	A	23	5	B

Table 8 continued

Table 8 (*continued*)

Cluster	Star	EqW (mÅ)	$A(\text{Li})$ (dex)	$A(\text{Li})_{\text{NLTE}}$ (dex)	$\sigma_{A(\text{Li})}$ ^a (dex)	Quality	$^{12}\text{C}/^{13}\text{C}$	$\sigma_{^{12}\text{C}/^{13}\text{C}}$ ^b	Quality
NGC 6583	50	22.5	1.06	1.23	0.22	A	22	5	A
NGC 6583	62	21.5	0.96	1.14	0.22	A	23	5	A
NGC 6583	72	61.4	1.50	1.67	0.24	A	31	5	C
NGC 6583	92	41.3	1.36	1.52	0.18	A	27	5	A

^a Values of 0.0 refer to upper limits.

^b Values of 0.0 refer to lower limits.

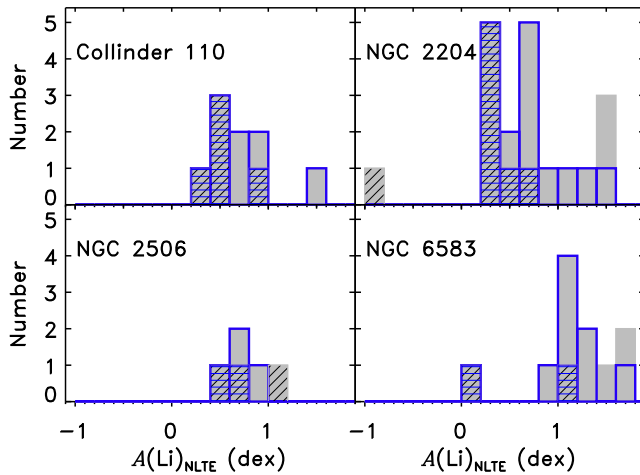


Figure 5. The distribution of the non-LTE $A(\text{Li})$ for all stars observed in each cluster (shaded gray histograms) and the subset of candidate RC stars (open blue histograms). The hatched regions denote stars with only upper limits on $A(\text{Li})$ in the full sample (diagonal lines) and the RC sample (horizontal lines).

5. DISCUSSION

5.1. Lithium Distribution

In Figure 5, we show the distribution of $A(\text{Li})_{\text{NLTE}}$ for the four clusters in this study, with histograms for both the full observed sample and the subset of RC candidate stars. The non-RC stars tend to fall at either extremes of the distributions, but are more commonly at the high extreme. For three of the clusters, the majority of the RC candidates fall into a single distribution that peaks around ~ 0.7 dex and is composed of mostly upper limit measurements. Two of those clusters (Collinder 110 and NGC 2204) have RC candidates in a second group or tail that extends into the Li-rich regime. In contrast, the fourth cluster (NGC 6583, both the most-metal rich and youngest cluster in this study) shows a peak in the distribution at much higher $A(\text{Li})$ with very few upper limit measurements. Only a single RC star has significantly lower $A(\text{Li})$.

These bimodal-like lithium distributions are similar to three clusters with $A(\text{Li})$ dichotomies reported previously in the literature for NGC 752, NGC 3680, and IC 4651 (Pilachowski et al. 1988, Pasquini et al. 2001, Pasquini et al. 2004). All three clusters have similar ages (1.5–1.9 Gyr) and are older than two of our clusters (NGC 6583 and Collinder 110) but younger than the other two (NGC 2204 and NGC 2506). The dichotomy of $A(\text{Li})$ in these three literature clusters has been interpreted as discriminating between first ascent RGs and RC stars in each cluster, with the higher $A(\text{Li})$ corresponding to the former, and lower $A(\text{Li})$ to the latter. This interpretation is also borne out in Collinder 110 and NGC 2204, where it is clear from Figure 2 that the highest Li stars (filled symbols) are the ones that appear to be first ascent RGB stars and not RC stars.

However, because RC should be more common than first ascent RGs, one would expect all of the clusters to have more low $A(\text{Li})$ stars than high $A(\text{Li})$ stars. This is not the case for NGC 3680 (or NGC 6583 in this work), which led Pasquini et al. (2001) to suggest that the high $A(\text{Li})$ stars in NGC 3680 were in fact the RC stars. An expanded sample of giants in NGC 3680 by Anthony-Twarog et al. (2009) confirmed this Li dichotomy. NGC 3680 is the oldest and most metal-poor ($[\text{Fe}/\text{H}] \sim -0.14$ dex) of those three literature clusters, but NGC 6583 is the youngest and most metal-rich of the clusters studied here. Since we have previously estimated evolutionary stages for our cluster stars, we can explore the Li distribution of each cluster in more detail. In Figure 6, we show $A(\text{Li})$ as a function of V magnitude and $^{12}\text{C}/^{13}\text{C}$. In general, the RGB stars (identified as squares) show the largest abundances, while the candidate RC stars (triangles) show depleted abundances. This is true even in NGC 6583; the RC stars have depleted $A(\text{Li})$ compared to the first ascent RGB stars, but the depletion in this cluster is less than that in the other three clusters. The apparent dichotomous $A(\text{Li})$ distribution in this cluster is in fact three different lev-

els of $A(\text{Li})$: RGB stars with the least Li dilution, RC stars with moderate Li dilution, and one RC star with significant dilution.

Our four cluster sample suggests that if Li-replenishment is commonly occurring at the He flash, the subsequent destruction of Li reduces the surface abundance below the RGB levels. A few outliers are worth noting. First, in NGC 6583 the most luminous star has $A(\text{Li})$ comparable to the other RGB star, whereas the most luminous star in NGC 2204 has severely depleted levels. This implies that the NGC 2204 luminous star is on the AGB, not the RGB. In all of the clusters except NGC 2506, there are one or more candidate RC stars with $A(\text{Li})$ more similar to the RGB star levels. RC stars are plotted as red circles in Figures 1 (which was used to determine their RC candidacy) and 2. We find that all but one of the candidate RC stars with high Li are closer matches to the first ascent RGB in Figure 2 and were reclassified based on those positions. The exception is NGC 6583 72, whose classification is ambiguous in Figure 2.

The second panel in Figure 6 shows $A(\text{Li})$ as a function of $^{12}\text{C}/^{13}\text{C}$. Most of the stars fall along a trend of decreasing $^{12}\text{C}/^{13}\text{C}$ with decreasing $A(\text{Li})$. This behavior is expected since both quantities are altered by mixing in stars. The stars along the linear trend follow the same distribution as the open cluster stars studied by Carlberg et al. (2016). There are again some exceptions. There is a grouping of eleven stars with low $^{12}\text{C}/^{13}\text{C}$ but $A(\text{Li}) \sim 0.6$ dex. Seven of these have limits in one of the parameters such that they could fall along the trend. Four stars, on the other hand, are still outliers. All of the stars are in the clusters that had the difficult telluric removal, so it is possible that the low $^{12}\text{C}/^{13}\text{C}$ measurements are spurious. However, our confidence in the validity of the measurements are due to the facts that (1) the ^{13}CN feature is stronger (more easily detectable) for low $^{12}\text{C}/^{13}\text{C}$, and (2) owing to the blend of lines creating the ^{13}CN feature, the width of the line would be difficult to mimic with residuals from the telluric removal.

5.2. Test of the He Flash Li Enrichment Mechanism

This sample of stars was selected specifically to test the hypothesis that Li is generated at the He flash. In the K11 sample, all of the Li-rich stars that have $^{12}\text{C}/^{13}\text{C}$ available have $A(\text{Li}) > 1.98$ dex. This minimum $A(\text{Li})$ in the K11 sample is influenced by two factors. First, the newly discovered RGs in K11 were pre-screened for the presence of the Li line in low resolution spectra, leading to a temperature-dependent minimum $A(\text{Li})$. Second, the lowest $A(\text{Li})$ stars in both the new RG and literature RG samples in K11 do not have $^{12}\text{C}/^{13}\text{C}$ measurements. None of our stars have

Li abundances at this level, implying a low occurrence rate for Li-rich stars. Using the binomial statistics in Burgasser et al. (2003), we can estimate the 1σ upper bound for the occurrence rate of RC clump stars more Li-rich than 1.98 dex to be $< 5\%$. This result is the same if we use all 38 photometrically identified RC candidates or if we reduce the sample size to 35 to account for the ones that may be RGB stars. The lack of a Li-rich star in our sample is still consistent with the K11 field giant study, which estimated the incidence to be around 1%.

If we factor $^{12}\text{C}/^{13}\text{C}$ into our consideration, we can perform a more stringent test of the fraction of stars that go through a Li-enriched phase early in the core He-burning stage. In Figure 7, we show the $^{12}\text{C}/^{13}\text{C}$ distribution of the subset of the K11 sample that overlaps our RC sample in parameter space. We remove stars from the K11 paper that have $\log L/L_\odot > 2.5$ and $T_{\text{eff}} < 4750$ K. The first cut removes four luminous RGs in K11 that are outside of the mass range and are near the second dredge-up phase on the early-AGB (see Charbonnel & Balachandran 2000). The second cut removes cooler RGs that are more likely to be at the luminosity bump. Overlaid in Figure 7 is the $^{12}\text{C}/^{13}\text{C}$ distribution of our sample of 38 RC candidates. The distributions are very different. The majority of the Li-rich K11 stars have $^{12}\text{C}/^{13}\text{C} \lesssim 10$. Such a low $^{12}\text{C}/^{13}\text{C}$ is a signature of deep mixing that dredges up material from the vicinity of the H-burning shell, where $^{12}\text{C}/^{13}\text{C}$ is 3.5 (Caughlan 1965). This implies that the mechanism responsible for the enhanced Li requires (or is accompanied by) very deep mixing. Because $^{12}\text{C}/^{13}\text{C}$ of the stellar atmosphere can only be lowered by mixing, this signature of low $^{12}\text{C}/^{13}\text{C}$ will persist even when the lithium levels return to normal low values. Therefore, the $^{12}\text{C}/^{13}\text{C}$ distribution of our RC sample is inconsistent with the hypothesis that most/all stars of 1.5–2.2 M_\odot experience a brief Li-rich stage. Instead, the Li-rich stage must only be experienced by a small fraction of stars.

We can identify the subset of stars in our sample that likely went through a Li-rich phase as the outlier group of low $^{12}\text{C}/^{13}\text{C}$ stars we identified in Figure 6. If the four stars that are clear outliers (i.e., no limit on either abundance measurement) are the only true outliers, then only $13.8\%_{-4.1\%}^{+8.7\%}$ of the RC stars went through a Li-rich phase. The fraction is larger if we include all 11 stars in the low $^{12}\text{C}/^{13}\text{C}$ outlier group, which results in an occurrence rate of $37.9\%_{-7.9\%}^{+9.5\%}$. The RC sample for these two calculations only use the RC candidates without strong evidence for reclassification (i.e., the ‘reclassified’ RC candidates in Collinder 110 and NGC 2204 are removed) and only considers stars with $^{12}\text{C}/^{13}\text{C}$ measurements. These constraints yield 29 RC stars.

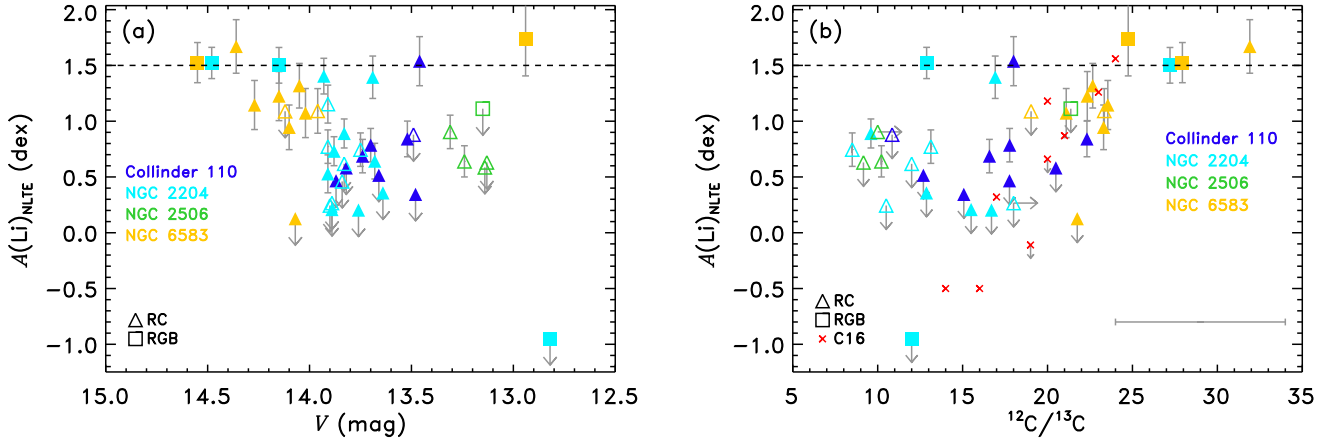


Figure 6. $A(\text{Li})_{\text{NLTE}}$ as a function of V magnitude (a), and $^{12}\text{C}/^{13}\text{C}$ (b). Triangles are RC candidates, while squares represent likely RGB stars. Arrows indicate limits. Filled symbols are the quality ‘A’ lithium measurements (most reliable), while open symbols are quality ‘B.’ In the second plot, the \times ’s show the results from [Carlberg et al. \(2016\)](#), and a representative error bar for $^{12}\text{C}/^{13}\text{C}$ is shown in the lower right.

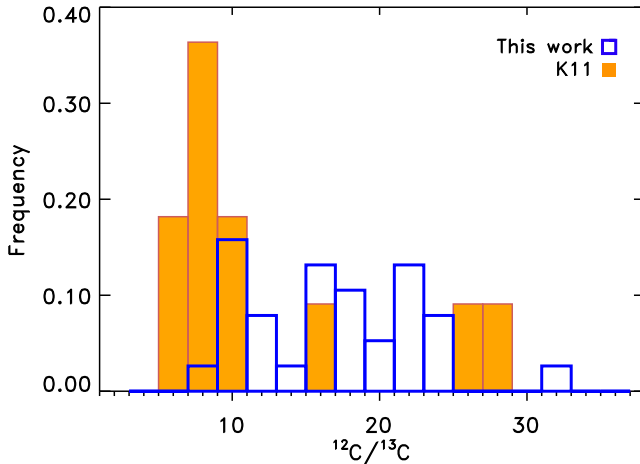


Figure 7. Distribution of $^{12}\text{C}/^{13}\text{C}$ in the 38 RC candidates in this work (open histogram) and for the Li-rich stars with $\log L/L_{\odot} < 2.5$ and $T_{\text{eff}} > 4750$ K in [K11](#) (filled histogram). The temperature and luminosity limits were imposed on the [K11](#) sample to restrict it to stars most similar to the RC stars in this work.

5.3. Confounding Factors: Stellar Rotation and Other Physics

Our interpretations may also be affected by the unknown rotational histories of the individual stars. The main sequence progenitors of the stars in the mass range we are studying have a large distribution of rotational velocities, with a typical value of 150 km s^{-1} ([Royer et al. 2007](#)). Despite this large variation on the MS, [Carlberg \(2014\)](#) showed that the red giant descendants of these stars are still almost uniformly slow rotators, a result that is reproduced here (Section 4.3). This fact makes it difficult to discern which stars were faster or slower MS rotators. The initial MS rota-

tion affects the depth of mixing and thus the observed surface $A(\text{Li})$ of RGs (see, e.g., [Lagarde et al. 2012](#)). Furthermore, rotation extends the main sequence lifetime ([Eggenberger et al. 2010](#)). In an effort to explain the extended MS turn-offs of clusters in the Magellanic Clouds, [Girardi et al. \(2011\)](#) explored the differences of isochrone morphology of models including large initial rotation compared to non-rotating models. They found that the isochrones made with fast rotating models were nearly indistinguishable from the slow rotating models. The implication to this work is that some of the RGs may be both more massive than we expect and may have experienced extensive rotational mixing. These stars would be difficult to distinguish from the stars that conform to the non-rotating model assumptions.

Among intermediate age Milky Way open clusters, some show extended RC morphologies that are inconsistent with simple single stellar population models ([Girardi et al. 2000](#)). Some of this extension is due to the fact that the ages of these clusters are such that the RC stars span the mass range that delineates the transition from quiescent to He flash core burning, resulting in a primary and secondary RC ([Girardi 1999](#)). However, this cannot explain all of the spread in the MSTO, nor can it be explained with an age spread ([Girardi et al. 2000](#)). The authors note that variations in the mass loss rate on the RGB or in the core overshoot efficiencies on the MS (which affects the mass transition for the different types of He core burning onset) could be responsible. If these factors are at play in the clusters of this work, they may also influence the variation of $A(\text{Li})$ observed in our clusters.

6. CONCLUSIONS

We have measured $A(\text{Li})$ and $^{12}\text{C}/^{13}\text{C}$ in a sample of RGs in four Southern open clusters. Most of the stars are RC stars having masses between 1.6 and 2.2 M_{\odot} , which were selected to test the hypothesis that stars in this mass range synthesize Li during the He flash and spend a short fraction of their RC lifetimes as Li-rich stars (K11). We find seven stars with $A(\text{Li})$ near the threshold of Li-richness at 1.5 dex. Three of these stars are RGB stars, and all of the four that were identified as candidate RC stars on CMDs are or could be consistent with the RGB on spectroscopic $T_{\text{eff}} - \log g$ diagrams.

Given the modest sample size, the absence of Li-rich stars in the RC constrains the occurrence (or fractional lifetime) to $< 5\%$, which is compatible with the 1% lifetime quoted by K11. However, the majority of the Li-rich RC field giants in K11 have low $^{12}\text{C}/^{13}\text{C}$, the result of deep mixing which dredges-up material with $^{12}\text{C}/^{13}\text{C}$ near 3.5. Even if the freshly synthesized Li is destroyed during the RC lifetime, the evidence of the past deep mixing (i.e., low $^{12}\text{C}/^{13}\text{C}$) should remain. The RC sample in this study has a $^{12}\text{C}/^{13}\text{C}$ distribution that is much higher, demonstrating that these stars experienced less mixing. We therefore conclude that if a Li-enrichment

episode occurs at the He flash, it must only affect a fraction of the stars evolving through that phase. From a set of outliers in the $A(\text{Li}) - ^{12}\text{C}/^{13}\text{C}$ distribution, we estimate that fraction to be $13.8\%_{-4.1\%}^{+8.7\%}$. Accounting for stars with uncertain evolutionary stage and limits in their abundances, we can set a conservative upper limit for the incidence to be $< 47\%$.

We are grateful to S. H. Lee and H. B. Ann for providing us their optical photometry of the NGC 2506 red giants in this study. We also thank the referee for valuable feedback that improved this manuscript. JKC acknowledges support by an appointment to the NASA Postdoctoral Program at the Goddard Space Flight Center, administered by Universities Space Research Association through a contract with NASA. This paper includes data gathered with the 6.5 m Magellan Telescopes located at Las Campanas Observatory, Chile and made use of the WEBDA database, operated at the Department of Theoretical Physics and Astrophysics of the Masaryk University.

Facility: Magellan:Clay (MIKE)

REFERENCES

- Adamów, M., Niedzielski, A., Villaver, E., et al. 2015, *A&A*, 581, A94
- Anthony-Twarog, B. J., Deliyannis, C. P., Twarog, B. A., Croxall, K. V., & Cummings, J. D. 2009, *AJ*, 138, 1171
- Balachandran, S. C., Fekel, F. C., Henry, G. W., & Uitenbroek, H. 2000, *ApJ*, 542, 978
- Bragaglia, A., & Tosi, M. 2003, *MNRAS*, 343, 306
- Bressan, A., Marigo, P., Girardi, L., et al. 2012, *MNRAS*, 427, 127
- Brown, J. A., Sneden, C., Lambert, D. L., & Dutchover, E. J. 1989, *ApJS*, 71, 293
- Burgasser, A. J., Kirkpatrick, J. D., Reid, I. N., et al. 2003, *ApJ*, 586, 512
- Busso, M., Wasserburg, G. J., Nollett, K. M., & Calandra, A. 2007, *ApJ*, 671, 802
- Cameron, A. G. W., & Fowler, W. A. 1971, *ApJ*, 164, 111
- Carlberg, J. K. 2014, *AJ*, 147, 138
- Carlberg, J. K., Cunha, K., Smith, V. V., & Majewski, S. R. 2012, *ApJ*, 757, 109
- Carlberg, J. K., Smith, V. V., Cunha, K., & Carpenter, K. G. 2016, *ApJ*, 818, 25
- Carraro, G., Méndez, R. A., & Costa, E. 2005, *MNRAS*, 356, 647
- Cassisi, S., Salaris, M., & Pietrinferni, A. 2016, *A&A*, 585, A124
- Caughlan, G. R. 1965, *ApJ*, 141, 688
- Charbonnel, C., & Balachandran, S. C. 2000, *A&A*, 359, 563
- Charbonnel, C., & Zahn, J.-P. 2007, *A&A*, 467, L15
- Denissenkov, P. A., Pinsonneault, M. H., & MacGregor, K. B. 2009, *ApJ*, 696, 1823
- Denissenkov, P. A., & Vandenberg, D. A. 2003, *ApJ*, 593, 509
- Eggenberger, P., Miglio, A., Montalbán, J., et al. 2010, *A&A*, 509, A72
- Eggleton, P. P., Dearborn, D. S. P., & Lattanzio, J. C. 2008, *ApJ*, 677, 581
- Friel, E. D., Janes, K. A., Tavaréz, M., et al. 2002, *AJ*, 124, 2693
- Ghezzi, L., Cunha, K., Smith, V. V., et al. 2009, *ApJ*, 698, 451
- Girardi, L. 1999, *MNRAS*, 308, 818
- Girardi, L., Eggenberger, P., & Miglio, A. 2011, *MNRAS*, 412, L103
- Girardi, L., Mermilliod, J.-C., & Carraro, G. 2000, *A&A*, 354, 892
- Hekker, S., & Meléndez, J. 2007, *A&A*, 475, 1003
- Hinkle, K., Wallace, L., Valenti, J. A., & Harmer, D. 2000, *Visible and Near Infrared Atlas of the Arcturus Spectrum 3727-9300 Å* (San Francisco, CA: ASP)
- Houdashelt, M. L., Bell, R. A., & Sweigart, A. V. 2000, *AJ*, 119, 1448
- Jacobson, H. R., Friel, E. D., & Pilachowski, C. A. 2011, *AJ*, 141, 58
- Kassis, M., Janes, K. A., Friel, E. D., & Phelps, R. L. 1997, *AJ*, 113, 1723
- Kelson, D. D. 2003, *PASP*, 115, 688
- Kim, S.-L., Chun, M.-Y., Park, B.-G., et al. 2001, *AcA*, 51, 49
- Kumar, Y. B., & Reddy, B. E. 2009, *ApJL*, 703, L46
- Kumar, Y. B., Reddy, B. E., & Lambert, D. L. 2011, *ApJL*, 730, L12
- Lagarde, N., Decressin, T., Charbonnel, C., et al. 2012, *A&A*, 543, A108
- Lee, S. H., Kang, Y.-W., & Ann, H. B. 2012, *MNRAS*, 425, 1567
- Lind, K., Asplund, M., & Barklem, P. S. 2009, *A&A*, 503, 541
- Magrini, L., Randich, S., Zoccali, M., et al. 2010, *A&A*, 523, A11
- Massarotti, A., Latham, D. W., Stefanik, R. P., & Fogel, J. 2008, *AJ*, 135, 209
- Ramírez, I., & Meléndez, J. 2005, *ApJ*, 626, 465
- Mermilliod, J.-C., & Mayor, M. 2007, *A&A*, 470, 919
- Mermilliod, J. C., Mayor, M., & Udry, S. 2008, *A&A*, 485, 303
- Mikolaitis, Š., Tautvaišienė, G., Gratton, R., Bragaglia, A., & Carretta, E. 2011, *MNRAS*, 416, 1092
- Neuforge-Verheecke, C., & Magain, P. 1997, *A&A*, 328, 261
- Pancino, E., Carrera, R., Rossetti, E., & Gallart, C. 2010, *A&A*, 511, A56

- Pasquini, L., Randich, S., & Pallavicini, R. 2001, *A&A*, 374, 1017
- Pasquini, L., Randich, S., Zoccali, M., et al. 2004, *A&A*, 424, 951
- Pilachowski, C. A., Saha, A., & Hobbs, L. M. 1988, *Astronomical Society of the Pacific*, 100, 474
- Plez, B. 2008, *Physica Scripta*, 133, 4003
- Royer, F., Zorec, J., & Gómez, A. E. 2007, *A&A*, 463, 671
- Silva-Aguirre, V., Ruchti, G. R., Hekker, S., et al. 2014, *ApJL*, 784, L16
- Snedden, C. 1973, *ApJ*, 184, 839
- U. S. Government Printing Office 2006, *The Astronomical Almanac for the year 2008*, (Washington, DC: USGPO)